

A Fast and Generalizable Fourier Neural Operator-Based Surrogate for Melt-Pool Prediction in Laser Processing

Alix Benoit¹, Toni Ivas¹, Mateusz Papierz², Asel Sagingalieva², Alexey Melnikov², Elia Iseli^{1*}

¹Laboratory for Advanced Materials Processing, Swiss Federal Laboratories for Materials Science and Technology, Feuerwerkerstrasse, Thun, 3603, BE, Switzerland.

²Terra Quantum AG, Kornhausstrasse, St. Gallen, 9000, SG, Switzerland.

*Corresponding author(s). E-mail(s): elia.iseli@empa.ch;

Abstract

High-fidelity simulations of laser welding capture complex thermo-fluid phenomena, including phase change, free-surface deformation, and keyhole dynamics, however their computational cost limits large-scale process exploration and real-time use. In this work we present the Laser Processing Fourier Neural Operator (LP-FNO), a Fourier Neural Operator (FNO) based surrogate model that learns the parametric solution operator of various laser processes from multiphysics simulations generated with FLOW-3D WELD[®]. Through a novel approach of reformulating the transient problem in the moving laser frame and applying temporal averaging, the system results in a quasi-steady state setting suitable for operator learning, even in the keyhole welding regime.

The proposed LP-FNO maps process parameters to three-dimensional temperature fields and melt-pool boundaries across a broad process window spanning conduction and keyhole regimes using the non-dimensional normalized enthalpy formulation. The model achieves temperature prediction errors on the order of **1%** and intersection-over-union scores for melt-pool segmentation over **0.9**. We demonstrate that a LP-FNO model trained on coarse-resolution data can be evaluated on finer grids, yielding accurate super-resolved predictions in mesh-converged conduction regimes, whereas discrepancies in keyhole regimes reflect unresolved dynamics in the coarse-mesh training data.

These results indicate that the LP-FNO provides an efficient surrogate modeling framework for laser welding, enabling prediction of full three-dimensional fields and phase interfaces over wide parameter ranges in just tens of milliseconds, up to a hundred thousand times faster than traditional Finite Volume multi-physics software.

Keywords: Laser melting, Physics-informed neural networks, Fourier neural operator, Multi-physics simulation.

1 Introduction

Welding has long been a fundamental manufacturing process across many industrial sectors. Among the available techniques, laser welding has gained particular importance due to its ability to process dissimilar materials, deliver highly localized and precisely controlled heat input, operate at high speeds, and enable non-contact, easily automated processing in geometrically constrained regions. However, laser welding involves strong multi-physics effects like transient heat transfer, fluid flows in the melt-pool, phase changes, free surface deformations, to name a few. The many influencing parameters create a strong need for fast and accurate numerical simulations to understand and optimize the quality of these processes.

Traditionally, methods such as the Finite Volume Method (FVM) and the Finite Element Method (FEM) have been used, which provide accurate solutions and have become robust and widely used in industry [1–3]. They can yield temperature fields, melt pool shapes, solidification patterns, and other characteristics which can then be validated experimentally. However, these methods can be extremely slow and computationally expensive, especially with fine meshes, strong melt-pool gradients, deep vapor depressions (keyholes), long tracks and multiple passes [4]. This computational cost can become especially problematic for process control, or for situations with many parameter changes involved such as process optimization and uncertainty quantification. There exist some simplified models such as diffusion only models which can have faster run-times, but usually they have to compromise physical accuracy and can only be used for a limited set of conditions. These models frequently employ a simplified approach within the framework of thermal-only models. This method approximates the complex effects of melt pool convection by using an effective thermal conductivity [5–7], while still suffering from the same problems as aforementioned models. Therefore there is a strong need for fast surrogate models which can retain high fidelity to the physical process of laser welding and can be used in a broad range of varying process parameters.

With the recent advances in Machine Learning (ML), work has been done to fill this gap through ML based surrogate models [8–10]. One approach has been to incorporate the underlying physics into either the architecture of neural networks, or into their loss functions, creating physics informed neural networks (PINNs). PINNs have successfully been applied to some welding and additive manufacturing (AM) problems. For example [11] gives an overview of some of the recently published AM related

work using PINNs, however it remains largely confined to the conduction (no vapor depressions) regime. Furthermore, a major drawback of standard PINNs is that they are typically trained to approximate the solution of a single PDE instance, that is for fixed parameters, geometry, boundary/initial conditions. As a result, when one changes the PDE parameters, geometry or boundary conditions, the network generally must be retrained (or at least substantially adapted). Additionally, PINNs can be difficult to optimize (balancing multiple loss terms, dealing with multi-scale phenomena, dynamic/time-dependent problems, stiff residuals) which limits their scalability to complex multi-physics or large parameter space settings [12] [13].

Instead of trying to approximate the solution of a PDE instance directly with a neural network, one can approximate the PDE family operator which maps input functions defining the PDE family (boundary conditions, material parameters, arbitrary coefficients, etc.) to corresponding solution fields. Such a model is called a neural operator (NO). Crucially, NOs are trained on many different PDE solution fields, and can therefore generalize to new parameter sets or geometries without retraining. Currently there exist various NO architectures, such as DEEPONET, Fourier NO (FNO), Graph NO (GNO) and Convolutional NO (CNO) [8, 14–16]. The strength of NOs is that once trained, they can give near instantaneous, physically consistent predictions of complete fields across wide parameter ranges. Such a model would be invaluable for applications such as laser welding, where real-time process control through a digital twin (DT), rapid process finding and optimization could strongly benefit or even only be enabled by this approach.

There has already been some work done in this direction. In [17] a neural network is presented to infer temperature field, gradients, and melt-pool shape, but only on a 2D slice. In [18] an example is given of an FNO based digital twin for Laser Powder Bed Fusion (L-PBF) process control. The underlying model however does not consider fluid dynamics or surface deformation. In [19] DEEPONET and PINNs are used to simulate multi-track L-PBF processes, but only conduction is considered. And finally, [20] combined FNO and DEEPONET for modeling bead volume (volume of deposited material) and maximum melt-pool temperatures in Direct Energy Deposition (DED) processes, but likewise focuses on the conduction regime, consistent with the intended DED scope.

In this work, we present the Laser Processing Fourier Neural Operator (LP-FNO), an FNO based model for predicting melt-pool characteristics in laser processing by considering heat and fluid dynamics. Training data are generated from high-fidelity thermo-fluid simulations of single-track laser scans on Ti-6Al-4V, spanning a broad process window in laser power and scan speed. The dataset covers multiple welding regimes, ranging from conduction modes to "stable" keyhole welding. To enable efficient operator learning, the problem is reformulated in a reference frame moving with the laser, allowing the governing dynamics to be treated in a quasi-steady setting. Once trained, the proposed LP-FNO directly maps process parameters to three-dimensional temperature fields and melt-pool geometries in a fraction of a second, up to a hundred thousand times faster than the traditional FVM equivalent. To the best of our knowledge, this is the first surrogate modeling approach that spans conduction and keyhole welding regimes while treating keyhole dynamics within a

quasi-steady operator-learning framework via time averaging. We employ a parameter sampling strategy through the notion of normalized enthalpy [21], which provides a generalizable mapping covering the different welding regimes evenly.

2 Methodology

2.1 Physical Model and Data Generation

In this work Ti-6Al-4V was used as material. The introduction of non-dimensional parameter variation (see below) however was used as a first step towards model generalization not limited to a single material.

Simulation Software.

The first step to build our surrogate FNO model is to choose high-fidelity simulations as ground truth to train the model. The laser melting process was simulated using a coupled multi-physics framework implemented in the commercial software FLOW-3D WELD[®] 2025R1 [22]. While experimental measurements could in principle be used as ground truth, this study relies exclusively on simulation data to avoid the additional cost and complexity associated with experiments. Evaporation is modeled through the added recoil pressure source term in the Navier–Stokes equations, an approach commonly used in previous studies [23, 24] because it substantially reduces computational cost [25] compared to fully compressible multiphase formulations [26], while retaining sufficient accuracy for predicting melt pool dynamics. FLOW-3D WELD[®] solves the Navier–Stokes equations with free-surface tracking using the Volume of Fluid (VoF) method, incorporating surface tension, recoil pressure, and heat transfer with phase change, and has been extensively validated in both industrial and academic contexts [27–29]. In the VoF formulation, each computational cell is assigned a volume fraction α (also referred to as solid fraction or metal-gas interface) representing the proportion of molten metal, with $\alpha = 1$ in the metal phase, $\alpha = 0$ in the gas phase, and intermediate values at the interface; this field is used as an important output to reconstruct the melt pool geometry. Thermal and fluid dynamics are coupled via temperature-dependent Marangoni convection and evaporation-induced recoil pressure, while laser energy absorption variations due to evolving keyhole geometry are accounted for using a ray-tracing approach. Thermophysical properties are taken from the FLOW-3D[®] database, with the surface tension set to 1.65 kg/s^2 and a temperature coefficient of $-2.4 \times 10^{-4} \text{ kg/s}^2/\text{K}$ [30]. The computational domain is defined as a $0.9 \text{ mm} \times 0.4 \text{ mm} \times 0.3 \text{ mm}$ rectangular cuboid (length, width, height), discretized with a uniform Cartesian mesh of $10 \text{ }\mu\text{m}$ resolution. A pressure boundary condition with 1 atm was used on the top surface, and on every other boundary, a temperature of 300 K was imposed. Laser scanning is modeled as a Gaussian laser source of radius $50 \text{ }\mu\text{m}$ moving along the length direction. The simulation results are written at every time step of $5 \text{ }\mu\text{s}$. The total simulation time is set based on the scan speed such that the laser travels exactly 0.6 mm. The reference change and time averaging processes are described in Section 2.3.

Process Parameter Variations.

While in principle any process or material parameter could be varied, we choose to vary laser scan speed V_{scan} and laser power P with ranges $V_{scan} \in [0.1, 1]$ m/s and $P \in [40, 190]$ W, in order to cover the different melting regimes, lack of fusion (LoF), conduction melting and keyhole.

To decide how to sample the points within these ranges we first introduce the concept of normalized enthalpy [21]. Normalized enthalpy H^* is a non-dimensional number that describes the keyhole formation threshold, defined in Equation 1 with values from Table 1. What is mainly important for us is that $H^* \propto \frac{P}{\sqrt{V_{scan}}}$. In order to have similar representation for both keyhole and conduction regimes, we sample our data on an equally spaced grid in H^* and P , and derive the corresponding V_{scan} from Equation 1. We then select validation, and testing samples (used to evaluate super-resolution accuracy) so as to span all H^* values, to make sure all regimes from LoF to keyhole are accounted for, as we can see in Figure 1. One can see an example of a conduction regime simulation in Figure 8 and a keyhole regime in Figure 9.

$$H^* = \frac{\eta P}{\rho C_p \Delta T_m \sqrt{\pi} D \sigma^3 V_{scan}} \quad (1)$$

| Symbol | Value | Description |
|--------------|--|---|
| η | 0.35 | Absorptivity |
| ρ | 4420 kg/m ⁻³ | Density (*) |
| C_p | 750 J/kg/K | Specific heat capacity (**) at Tsolidus=1873K |
| ΔT_m | 1573 K | Temperature rise to melting |
| D | 8.1×10^{-6} m ² /s | Thermal diffusivity (**) |
| σ | 50 μ m | Beam radius (1/e ²) |
| P | 40–190 W | Laser power range |
| V_{scan} | 0.1–1 m/s | Scan speed range |

Table 1 Parameters used for normalized enthalpy evaluation. (*) Parameter taken at $T = 298$ K. (**) Parameter taken at Tsolidus=1873K

2.2 The Fourier Neural Operator

The classical Fourier Neural Operator architecture is used, which is described for modeling the laser melting, in the following section. One can see an overview diagram of the LP-FNO in Figure 2.

Mathematical Setting.

A class of steady (time-independent) partial differential equations posed on a bounded domain $D \subset \mathbb{R}^d$ is assumed. The problem is written in operator form as follows:

$$\begin{cases} \mathcal{P}(u, a) = 0, & \text{in } D, \\ u = g, & \text{on } \partial D, \end{cases} \quad (2)$$

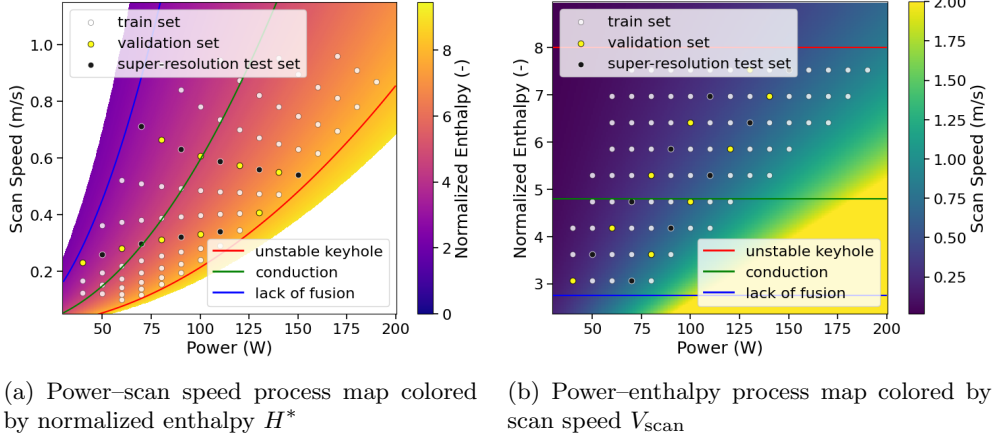


Fig. 1 Process-space coverage of high-fidelity simulation data generated with FLOW-3D WELD. The dataset spans laser power P and scan speed $V_{\text{scan}} \in [0.1 \text{ m s}^{-1}, 1.0 \text{ m s}^{-1}]$, and is constructed on a grid uniform in normalized enthalpy H^* and power. Markers denote the training, validation, and super-resolution test sets used for neural operator learning

where $u \in \mathcal{U}$ denotes the unknown solution field and $a \in \mathcal{A}$ represents a set of input parameters, typically corresponding to spatially varying coefficients, source terms, or material properties of the PDE. In our case u is the concatenation of temperature field T , the volume fraction α , and the fluid fraction $f_l(T)$ (defined in section 2.3), and the variable parameter field is $a = (P, V_{\text{scan}})$, it is thus constant in space. The boundary conditions g are described in the previous section.

The operator $\mathcal{P} : \mathcal{U} \times \mathcal{A} \rightarrow \mathcal{F}$ denotes the differential operator defining the PDE, with \mathcal{U} , \mathcal{A} , and \mathcal{F} taken as Banach spaces equipped with appropriate norms. Under standard well-posedness assumptions, the PDE admits a unique solution for each admissible parameter field a .

Solution Operator.

This setting induces a solution operator

$$\mathcal{G}^\dagger : \mathcal{A} \rightarrow \mathcal{U}, \quad a \mapsto u, \quad (3)$$

which maps the PDE parameters directly to the corresponding solution. The goal of operator learning is to approximate \mathcal{G}^\dagger from data, rather than learning a solution for a fixed instance of a .

For our case.

In this work, the governing equations are the Navier-Stokes equations, and the heat equation with added laser source in the laser frame of reference, along with the VoF

equation [25].

$$\frac{\partial \alpha}{\partial t} + \nabla \cdot (\alpha \mathbf{U}) = 0, \quad (4)$$

Where α is the volume fraction and U is the velocity field (not explicitly computed in our case). We look for stationary solutions of the equations, as part of our quasi-steady state assumption.

The FNO is employed to learn an approximation of the solution operator \mathcal{G}^\dagger that is resolution-invariant and defined directly at the operator level, enabling generalization across different resolutions of the domain discretization. The exact description of the governing equations is not necessary as they are learned implicitly by the neural operator through the parameter-solution pairs during training.

Discretized operator learning problem.

In practice, the parameter field $a(\mathbf{x})$ and the corresponding solution field $u(\mathbf{x})$ are observed on a grid (the FNO can be extended to non-cartesian meshes [31], but we still do the classical formulation here). Let D_h denote a discretization of D with N points (e.g., $N = n_x n_y n_z$ for a structured mesh in 3D), then the training dataset is given by pairs:

$$\left\{ (a^{(j)}|_{D_h}, u^{(j)}|_{D_h}) \right\}_{j=1}^N, \quad (5)$$

where each pair corresponds to one quasi-steady simulation instance. The learning task is to construct a parametric operator \mathcal{G}_θ such that $\mathcal{G}_\theta(a) \approx \mathcal{G}^\dagger(a)$, and such that the approximation remains meaningful when evaluated on a different discretization $D_{h'}$ (i.e., generalization across resolutions).

Architecture overview.

The FNO approximates \mathcal{G}^\dagger using a composition of L operator layers acting on a latent field. The construction is typically expressed as

$$\mathcal{G}_\theta = \mathcal{Q} \circ \mathcal{K}^{(L)} \circ \dots \circ \mathcal{K}^{(1)} \circ \mathcal{P}, \quad (6)$$

where \mathcal{P} denotes an input “lifting” map into a higher-dimensional channel space, $\mathcal{K}^{(\ell)}$ are Fourier layers, and \mathcal{Q} is an output projection back to the physical quantity of interest. An initial latent representation is then formed by

$$v_0(\mathbf{x}) = \mathcal{P}(a(\mathbf{x}), \mathbf{x}), \quad (7)$$

where $\mathbf{x} = (x, y, z)$ denotes the spatial coordinate.

Fourier layer as global convolution.

Each Fourier layer is designed to mix information over the entire domain efficiently, which is important for problems where long-range coupling is present. The update at layer ℓ is written point-wise in physical space as

$$v_{\ell+1}(\mathbf{x}) = \sigma((\mathcal{W}_\ell v_\ell)(\mathbf{x}) + (\mathcal{F}^{-1} \circ \mathcal{R}_\ell \circ \mathcal{F})[v_\ell](\mathbf{x})), \quad (8)$$

where σ denotes a nonlinearity (GELU [32] in our case), \mathcal{W}_ℓ is a learned point-wise linear map, and the second term implements a learned integral operator through the Fourier transform \mathcal{F} . This second term corresponds to a global convolution with a translation-invariant kernel; in Fourier space, such a convolution becomes multiplication by a mode-dependent operator.

Mode truncation and learnable spectral weights.

For a discretized field v_ℓ , the Fourier transform yields coefficients $\widehat{v}_\ell(\mathbf{k})$ indexed by wave-vectors \mathbf{k} . In practice, the Fourier-space operator \mathcal{R}_ℓ is implemented as a block-diagonal operator, where each retained Fourier mode \mathbf{k} is associated with a learnable matrix $\mathbf{R}_\ell(\mathbf{k})$ acting on the channel dimension. In the FNO, only a fixed set of low-frequency modes is retained:

$$\widehat{v}_{\ell+1}(\mathbf{k}) = \begin{cases} \mathbf{R}_\ell(\mathbf{k}) \widehat{v}_\ell(\mathbf{k}), & \mathbf{k} \in \mathcal{K}_m, \\ 0, & \text{otherwise,} \end{cases} \quad (9)$$

where \mathcal{K}_m denotes the retained index set (e.g. the first $m_1 \times \dots \times m_d$ modes). The truncation reflects the empirical observation that many PDE solution operators are well-approximated by their low-frequency content, while higher frequencies are either weakly excited or dominated by discretization noise. Computationally, the cost per layer scales as $\mathcal{O}(n \log n)$ due to the FFT, while the learnable spectral multiplication acts only on $\mathcal{O}(m_1 \dots m_d)$ modes.

Input/output maps and physical fields.

The lifting map \mathcal{P} and projection map \mathcal{Q} are typically implemented as pointwise multilayer perceptrons (MLPs). This design keeps the network compatible with variable grid sizes, which means that the same parameters are reused at each spatial location, and the Fourier mixing step is defined through FFTs on the current grid. For multiphysics settings, multiple input channels (e.g. power, scan speed, normalized enthalpy, and grid coordinates in our case) may be concatenated into $a(\mathbf{x})$, while multiple output channels may be predicted jointly (e.g. temperature, volume fraction, and liquid fraction in our case).

Training objective.

Training is performed using supervised pairs $(a^{(j)}, u^{(j)})$ by minimizing the empirical risk function:

$$\min_{\theta} \frac{1}{N} \sum_{j=1}^N \left\| \mathcal{G}_\theta(a^{(j)}) - u^{(j)} \right\|_{\mathcal{U}_h}^2, \quad (10)$$

where $\|\cdot\|_{\mathcal{U}_h}$ denotes a discretized norm (in our case L^2 norm over grid points). When multiple fields are predicted, there are multiple ways to aggregate them, the most simple being a weighted sum. We opt for the ReLoBraLo [33] aggregator, which was specifically designed for PINNs.

Resolution invariance in practice.

The resolution-invariant behavior of the FNO is a consequence of (i) the point wise maps \mathcal{P} and \mathcal{Q} that do not depend on grid size and (ii) the Fourier mixing defined by a fixed set of retained modes (m_1, \dots, m_d) rather than a fixed number of grid points. As a result, the learned spectral weights $\mathbf{R}_\ell(\mathbf{k})$ for a specific mesh resolution can be applied on another mesh resolution, provided the retained Fourier indices are representable on the evaluation grid. For non-periodic domains or non-periodic boundary conditions, padding or other boundary treatments are applied before computing the FFT so that the spectral convolution remains numerically stable. In our case, while we have a periodic domain on some sides, most are equal to 300 K for the temperature field, the top side breaks periodicity; we thus employ a zero padding of size 9 around our domain boundary.

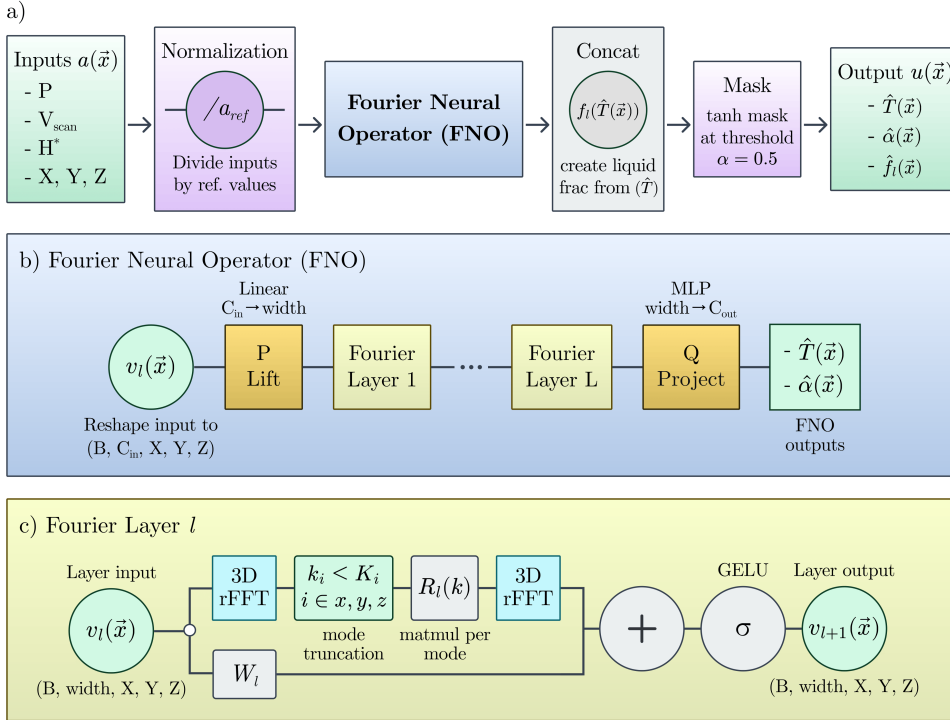


Fig. 2 Architecture of LP-FNO forward pass

2.3 Case specific processing

In order to use the FNO architecture for laser melting, different adjustments were made for consistent training.

Reference frame change.

To transform the data into the reference frame of a laser moving at a constant speed V_{scan} , the temporal sampling is chosen such that the laser displacement aligns exactly with the underlying uniform computational grid. Given a spatial grid with uniform spacing Δx , the time increment Δt is therefore selected so that the laser travels precisely one grid cell per time step,

$$\Delta t = \frac{\Delta x}{V_{scan}}. \quad (11)$$

With this choice, the laser position coincides with grid points at every time step in the moving reference frame, eliminating the need for spatial interpolation. Consequently, if the laser traverses a total distance corresponding to m grid cells, only m discrete time steps are retained in the transformed frame, yielding a total elapsed time of $m \Delta x/V$. This approach aligns with treating the laser's travel distance as the effective evolution parameter, since simulations are run until a specified distance is reached rather than for a fixed physical time. We subsequently refer to time steps in the laser reference frame through indices as $t_k = k\Delta t$, $k \in \mathbb{N}$.

Quasi-steadiness assumption and time averaging.

In the reference frame moving with the laser at constant speed, temporal variations in the temperature field and melt-pool interface were largely confined to small-scale interface fluctuations, with minimal contribution from large-scale melt-pool evolution. To evaluate whether these fields could be treated as quasi-static, we analyzed the temporal differences between consecutive snapshots in the moving frame.

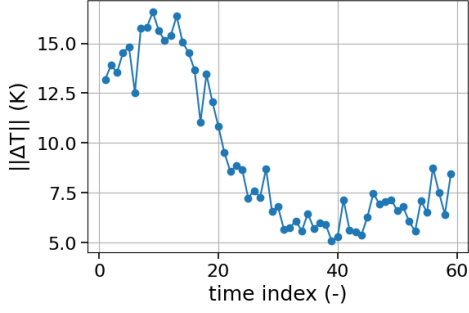
Figures 3 and 4 show the mean absolute difference between the temperature field at two successive time steps, $\|\Delta T(t_k)\| = \|T(t_k) - T(t_{k-1})\|$, for both conduction and keyhole welding regimes. Without temporal averaging, significant fluctuations persist in the keyhole regime (Figure 4a), reflecting the inherently unsteady dynamics of the vapor cavity and the associated melt-pool interface. In contrast, the conduction regime exhibits substantially smaller variations, indicating a closer proximity to steady behavior.

To isolate the large-scale, slowly varying structure of the melt pool, a temporal averaging procedure is applied over a sliding window, defined as

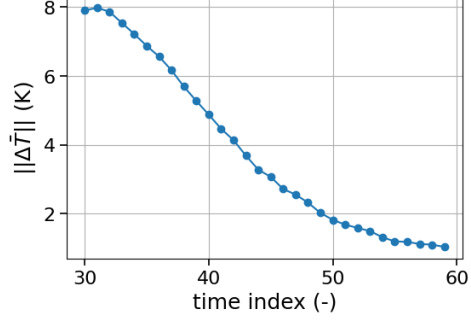
$$\bar{T}(t_k) = \frac{1}{n} \sum_{i=k-n}^k T(t_i), \quad (12)$$

with $n = 30$ time steps in the moving frame. After averaging, the magnitude of $\|\Delta \bar{T}(t_k)\|$ approaches zero in both regimes. This demonstrates that, once high-frequency interface oscillations are filtered out, the temperature field and melt-pool geometry exhibit only weak residual temporal dependence after the laser has traveled a sufficient distance.

These observations justify treating the melt pool as quasi-static in the laser reference frame, provided that an appropriate temporal averaging is employed.

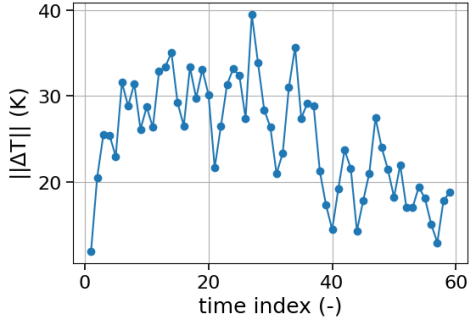


(a) No temporal averaging

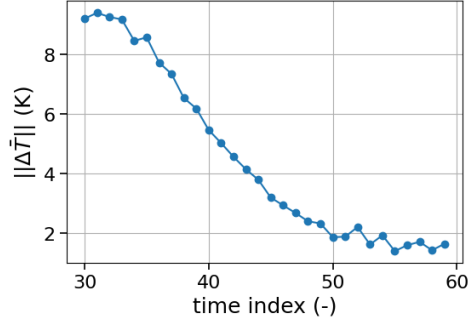


(b) Averaging over a 30-step window

Fig. 3 Conduction regime ($P = 70$, $V_{scan} = 0.298$, $H^* = 4.75$). Temporal evolution of the mean absolute temperature difference in the laser reference frame. Quasi-static behavior appears around $t = 30$ for non-averaged data, and in averaged data from $t_{avg} = 50$. Time averaging is defined in [Equation 12](#)



(a) No temporal averaging



(b) Averaging over a 30-step window

Fig. 4 Keyhole regime ($P = 150$, $V_{scan} = 0.542$, $H^* = 7.54$). Temporal evolution of the mean absolute temperature difference in the laser reference frame. Temporal averaging suppresses high-frequency interface fluctuations, revealing quasi-static behavior once the laser has traveled a sufficient distance. Time averaging is defined in [Equation 12](#)

Normalization of fields

All fields used by the LP-FNO were normalized by dividing by a typical reference value, so that they are all on the same order of magnitude to make learning easier. The used reference values are indicated in [Table 2](#).

Table 2 Reference values used for normalization

| Characteristic parameter | Symbol | Reference value |
|--------------------------|--------|--------------------------------|
| Length | L | 1×10^{-4} m |
| Temperature | T | 3000 K |
| Velocity | V | 1×10^{-1} m s $^{-1}$ |
| Power | P | 10 W |
| Normalized enthalpy | H | 7.5 |

Computation of liquid fraction.

The liquid fraction f_l is the amount in percentage which is liquid compared to solid and is defined as follows:

$$f_l(T(\mathbf{x})) = \begin{cases} 0, & T(\mathbf{x}) \leq T_s, \\ \frac{T(\mathbf{x}) - T_s}{T_l - T_s}, & T_s < T(\mathbf{x}) < T_l, \\ 1, & T(\mathbf{x}) \geq T_l. \end{cases} \quad (13)$$

where T_s and T_l are the solidus and liquidus temperatures of the metal respectively. For Ti-6Al-4V, $T_s = 1873$ K and $T_l = 1923$ K were used, based on the FLOW-3D[®] database. The region where $0 < f_l < 1$ is called the "mushy zone" [34]. In this regime, the solid dendrites and liquid metal coexist during phase transition like solidification or melting, and the fraction of the solid and liquid phases are determined by the phase diagram of the substance. In our case we assume that concentration variations are negligible and thermophysical and mechanical properties vary continuously with temperature. Although f_l is a thermodynamic quantity, in this work it is primarily used as a geometric indicator of the melt-pool boundary via thresholding at $f_l = 0.5$. The melt-pool region is thus defined by $\alpha(\mathbf{x}) \geq 0.5$ and $f_l(\mathbf{x}) \geq 0.5$. During the forward passes of the LP-FNO, f_l is computed from the inferred T field. It is then aggregated to the supervised loss for the backward pass in order to put extra emphasis on the network to learn the melt-pool boundary temperatures accurately.

Gas phase α -masking.

As the quantities of interest are confined to the metallic domain, and since FLOW-3D WELD[®] does not explicitly model the gas phase, a smooth masking procedure is applied to suppress fields in the surrounding gas phase. Specifically, the continuous volume fraction $\alpha(\mathbf{x}) \in [0, 1]$ is used to distinguish metal from gas, with $\alpha < 0.5$ indicating regions outside the metal. To preserve differentiability across the metal-gas interface, a smooth hyperbolic tangent gate is defined as

$$g(\mathbf{x}) = \frac{1}{2} [\tanh(k(\alpha(\mathbf{x}) - 0.5)) + 1], \quad (14)$$

where k controls the sharpness of the transition (we use $k = 20$). The temperature field is then smoothly blended toward a fixed value according to

$$\tilde{T}(\mathbf{x}) = T_{\text{boil}} + g(\mathbf{x})(T(\mathbf{x}) - T_{\text{boil}}), \quad (15)$$

with $T_{\text{boil}} = 3123$ K corresponding to the boiling temperature of Ti-6Al-4V. This operation is applied both after the forward pass of the network during inference and during pre-processing of the ground-truth data, preventing the introduction of spurious sharp gradients at the keyhole interface. In addition, the liquid fraction f_ℓ and inferred volume fraction $\hat{\alpha}(\mathbf{x})$ are masked to zero outside the metal, ensuring that they exclusively represents the melt-pool geometry.

Implementation.

We implemented FNO in Python using the PhysicsNeMo [35] package from NVIDIA with hyper-parameters described in Table 6 in Appendix A, and trained the model on FLOW-3D WELD[®] laser welding simulations as described in section 2.1. For training we implement the LION optimizer from [36].

K-folds cross validation

To evaluate the performance of the network, a validation subset was held out from the full dataset and used exclusively for hyperparameter tuning. Owing to the limited number of samples, the remaining data were evaluated using 8-fold cross validation. For each fold, the model was trained on 7/8 of the data and evaluated on the remaining 1/8, and the reported metrics correspond to averages aggregated across folds. To test super-resolution we used the classical train-validation-test set split from Figure 1 due to the high computational and storage costs of fine mesh reference multi-physics simulations. To generate the plots in Figure 6, 11, and 10, we used the full dataset with cross-validation, as the errors are reported on a per-simulation basis and any difference across validation folds would be readily apparent. The model converged across all outputs, both in terms of raw loss and in the test set per fold, which is shown in section A, Figure 12.

Metrics for model performance evaluation.

For evaluating the model performance the mean absolute error (MAE) was used which is defined as follows:

$$\text{MAE} = \frac{1}{N} \sum_{s=1}^N \left(\frac{1}{|D_h|} \sum_{\mathbf{x} \in D_h} |e^{(s)}(\mathbf{x})| \right), \quad (16)$$

as well as the root mean squared error (RMSE),

$$\text{RMSE} = \frac{1}{N} \sum_{s=1}^N \left(\sqrt{\frac{1}{|D_h|} \sum_{\mathbf{x} \in D_h} (e^{(s)}(\mathbf{x}))^2} \right). \quad (17)$$

where $y^{(s)}(\mathbf{x})$ denotes the ground-truth field and $\hat{y}^{(s)}(\mathbf{x})$ the predicted field for sample $s \in \{1, \dots, N\}$ on the discretized domain D_h with $|D_h|$ grid points. The point-wise error is defined as follows:

$$e^{(s)}(\mathbf{x}) = \hat{y}^{(s)}(\mathbf{x}) - y^{(s)}(\mathbf{x}). \quad (18)$$

In addition to the MAE and the RMSE, corresponding relative metrics were analyzed. For each output field, a normalization constant was defined as the global mean of the ground-truth values over the evaluation set,

$$\mu_y = \frac{1}{N |D_h|} \sum_{s=1}^N \sum_{\mathbf{x} \in D_h} y^{(s)}(\mathbf{x}), \quad (19)$$

and relative errors are computed as

$$\text{RelMAE} = \frac{\text{MAE}}{\mu_y + \varepsilon}, \quad \text{RelRMSE} = \frac{\text{RMSE}}{\mu_y + \varepsilon}, \quad (20)$$

with a small $\varepsilon > 0$ used for numerical stability.

For the solid fraction α and the liquid fraction f_l (which effectively defines the melt-pool boundary), the task can naturally be interpreted as a segmentation problem. Therefore additionally the intersection over union (IoU) was investigated. Given a threshold of $\tau = 0.5$, the predicted and ground-truth binary masks for sample s can be defined as:

$$\hat{M}^{(s)}(\mathbf{x}) = \mathbb{I}[\hat{y}^{(s)}(\mathbf{x}) \geq \tau], \quad M^{(s)}(\mathbf{x}) = \mathbb{I}[y^{(s)}(\mathbf{x}) \geq \tau], \quad (21)$$

and the IoU as follows:

$$\text{IoU} = \frac{1}{N} \sum_{s=1}^N \frac{\sum_{\mathbf{x} \in D_h} \hat{M}^{(s)}(\mathbf{x}) M^{(s)}(\mathbf{x})}{\sum_{\mathbf{x} \in D_h} \mathbb{I}[\hat{M}^{(s)}(\mathbf{x}) + M^{(s)}(\mathbf{x}) \geq 1]}. \quad (22)$$

Relative metrics were not computed for α and f_l since these fields are already dimensionless and consist largely of 0 valued points; thus, they are evaluated primarily through absolute errors and IoU.

3 Results and Discussion

Once the LP-FNO has been trained, we can generate the temperature field and melt-pool from any set of process parameters within the training range in a fraction of a second for any desired mesh resolution. For example, if we input the power $P = 150$ W and laser scanning speed $V_{scan} = 0.54$ m/s, we get the temperature field and melt-pool shown in [Figure 5](#) in around 10 ms for 10 μm resolution and in around 40 ms for 5 μm resolution. This is more than ten thousand times faster than the FLOW-3D[®]

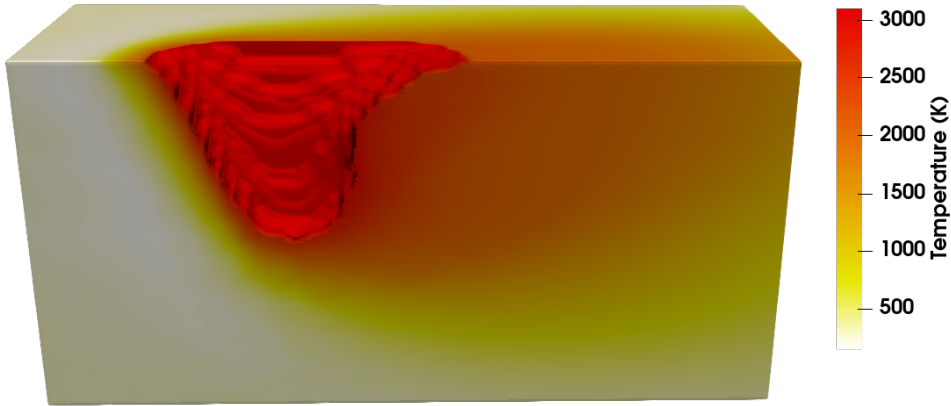


Fig. 5 LP-FNO 3D inference result for keyhole regime simulation with $P = 150$ W and $V_{scan} = 0.54$ m/s. Domain cut in half for visual clarity. Visualized using ParaView [37]

simulation equivalent at 10 ms resolution and around one hundred thousand times faster than FLOW-3D[®] at 5 ms resolution. One can see exact run-times for a given parameter set in Table 3.

Metrics across different parameter combinations for 10 μ m mesh.

Looking at how well our model performs over different parameter combinations, we first consider our metrics as a heat map over the entire parameter domain using K-folds to identify areas in the map where the model performs particularly well or poorly. We see in Figure 6 that there appears to be one outlier point at $P = 50$ W, $V_{scan} = 0.122$ m/s, which lies at edge of our data in start of conduction-keyhole transition. Looking more closely at the inference of α on that point in Figure 7, we see that as this is a transition point, the model is unsure as to whether this is a keyhole point or not, leading to some smearing of the interface and a spurious porosity prediction. This issue can easily be fixed by adding more training data around this point range. Other than at this point, the model performs quite strongly with most points on the map having an average temperature error of 10 K, with the error rising slightly to around 20 K at the high enthalpy keyhole region of the map, and at the low speed region, as anticipated due to the increased complexity of these regions and the lack of training data on the edges of the map. Looking at the segmentation of the melt-pool (f_i) in Figure 10 and the metal-gas interface α in Figure 11 in Appendix A, we see a similar

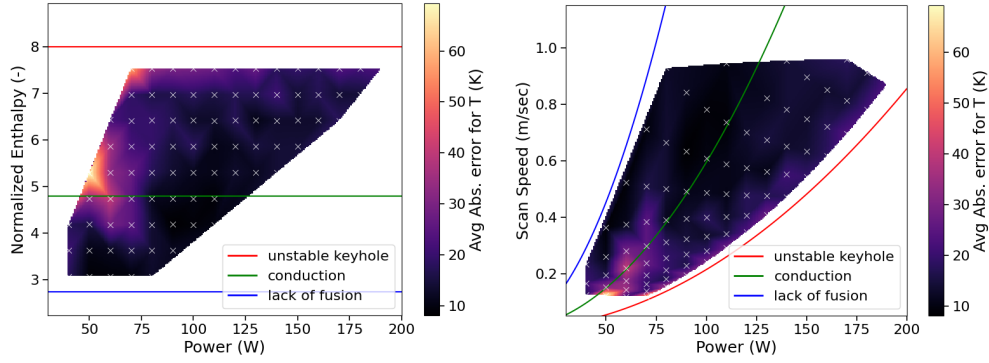
Table 3 Comparison of computational runtimes for high-fidelity FLOW-3D[®] simulations and LP-FNO surrogate modeling. FLOW-3D[®] runtimes correspond to a transient simulation (Power 50 W, Scan speed 0.260 m/s and scan distance of 0.6 mm), while LP-FNO runtimes include one-time training cost and per-sample inference cost. LP-FNO Inference was performed on an Ubuntu 24.04.3 LTS workstation with an Intel Core i9-10900X (10 cores / 20 threads), 125 GiB RAM, and dual NVIDIA TITAN RTX GPUs (24 GiB each), although only one GPU was used at a time. The FLOW-3D[®] simulations were run on a AMD Ryzen Threadripper 7960X using 16 cores

| Method | Mesh resolution | Runtime |
|---------------------------------|----------------------------|----------------|
| FLOW-3D [®] simulation | Coarse (10 μm) | 6 min 7 s |
| FLOW-3D [®] simulation | Fine (5 μm) | 1 h 6 min 54 s |
| LP-FNO training (6,000 steps) | Coarse (10 μm) | 7 min 24 s |
| LP-FNO inference | Coarse (10 μm) | 0.0100 s |
| LP-FNO inference | Fine (5 μm) | 0.0435 s |

pattern. The same outlier is present and the high enthalpy, keyhole edge of the map has higher error, except for the melt-pool IoU error. This is expected since the melt-pool is larger in the high enthalpy regime, which shrinks small segmentation errors in comparison to the same error in a small melt-pool. Similar reasoning explains why IoU errors in Figure 10c and 10d have comparatively large magnitudes, especially in the low speed and low enthalpy regimes, since melt-pools in those regimes can be very small, an error of even one voxel makes up a few percents of the total melt-pool and is thus amplified.

Table 4 FNO error metrics reported as mean and range [min, max] across 8-folds (without validation set used for hyperparameter tuning). Absolute temperature errors are reported in kelvin; relative errors are in percent. Relative metrics not reported for α and f_l as they are already dimensionless

| Metric | T (K) | Metal-Gas interface (α) | Melt-pool (f_l) |
|---------------|------------------|----------------------------------|------------------------|
| Abs. mean | 18.3 [14.1,21.3] | 0.0035 [0.0025,0.0048] | 0.0024 [0.0018,0.0034] |
| RMSE | 36.0 [30.0,45.0] | 0.017 [0.013,0.025] | 0.037 [0.030,0.045] |
| Rel. mean [%] | 2.9 [2.2,3.4] | – | – |
| Rel. RMSE [%] | 5.9 [5.0,7.2] | – | – |
| IoU mean | – | 0.9992 [0.9986,0.9992] | 0.91 [0.88,0.93] |
| IoU std | – | 0.00049 [0.00024,0.0011] | 0.053 [0.020,0.13] |



(a) Average absolute temperature error (Kelvin) as a function of laser power P and normalized enthalpy H^* (b) Average absolute temperature error (Kelvin) as a function of laser power P and scan speed V_{scan}

Fig. 6 Model error maps over the process parameter space. The color scale indicates the average absolute error for the predicted temperature field. Solid lines denote approximate regime indicators corresponding to lack of fusion (blue), conduction (green), and unstable keyhole (red). White markers indicate simulation samples used for training and evaluation with k-folds cross validation

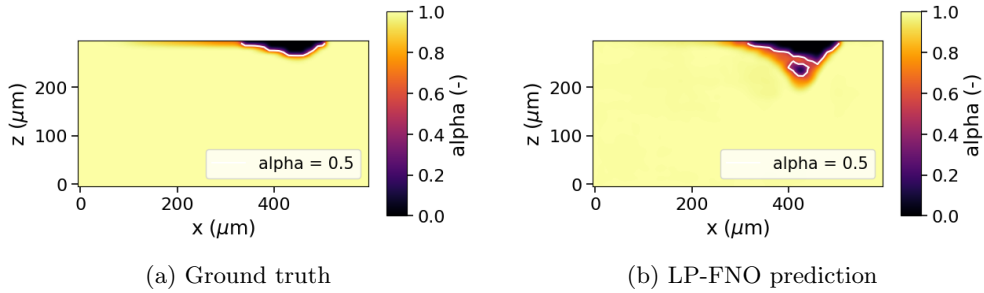


Fig. 7 Gas-metal interface (α) ground truth and FNO inference for an outlier case at $P = 50 \text{ W}$ and $V_{\text{scan}} = 0.122 \text{ m s}^{-1}$, where the model exhibits its largest deviation. While the overall interface geometry is well captured, a spurious gas bubble is erroneously inferred. This operating point lies close to the transition between conduction and keyhole regimes, where the model exhibits increased uncertainty. A few additional training data points in this region would likely greatly reduce this error

Average Metrics for 10 μm mesh.

Looking at our model performance more generally, from [Table 4](#), we see that our model performs, on average, quite well across all metrics. For the temperature field, we have an average absolute error of 18.3 K, or around 3 percent, and an RMSE of 36 K or 5.9 percent. For the metal-gas interface α we have a low average absolute error of 0.0035

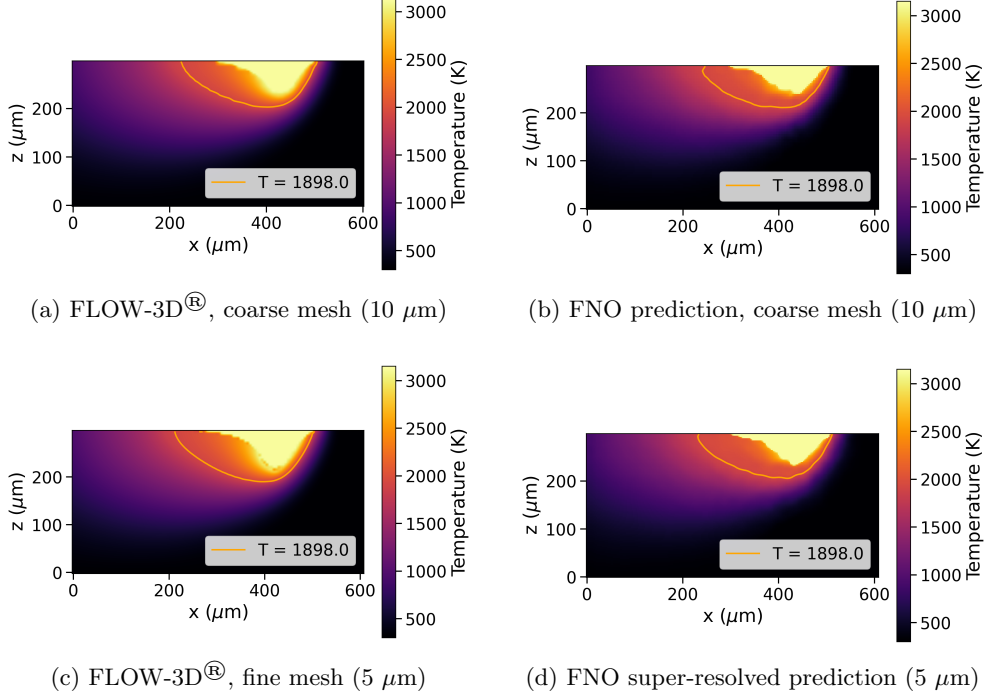


Fig. 8 Conduction-regime melt-pool mid-point cross-section comparison for a test case with $P = 70.0$ and $V_{\text{scan}} = 0.298 \text{ m s}^{-1}$. In contrast to the keyhole regime, the coarse and fine FLOW-3D[®] solutions are visually similar, indicating that mesh convergence is effectively achieved at 10 μm resolution in the conduction regime

with RMSE of 0.017 and a near perfect IoU of 0.9992. And for the full melt-pool segmentation we have an absolute error of 0.0024, an RMSE of 0.037, and an IoU of 0.91. The discrepancy between the α and f_l IoUs come from the fact that the melt-pool region denoted by f_l is much smaller than the full metal region denoted by α , so the IoU error gets proportionally bigger for f_l when compared to the one for α .

Super Resolution.

One of the strongest features of FNO is that as described in [section 2.2](#) it is resolution independent, meaning that we can train FNO on coarse simulation data, which is much faster to obtain (time and data size grow cubically with mesh refinement), and perform inference of the model on a much finer mesh. We evaluate our model trained on simulations with mesh size 10 μm on a representative sample with mesh size 5 μm covering all physical regimes from conduction to keyhole depicted by the test set points in [Figure 1](#). We do not run K-folds on the entire grid here due to high ground-truth data generation computational cost and size.

We can see the comparison between the coarse and fine mesh simulation and inference results for a conduction regime parameter set in [Figure 8](#) and for a keyhole regime

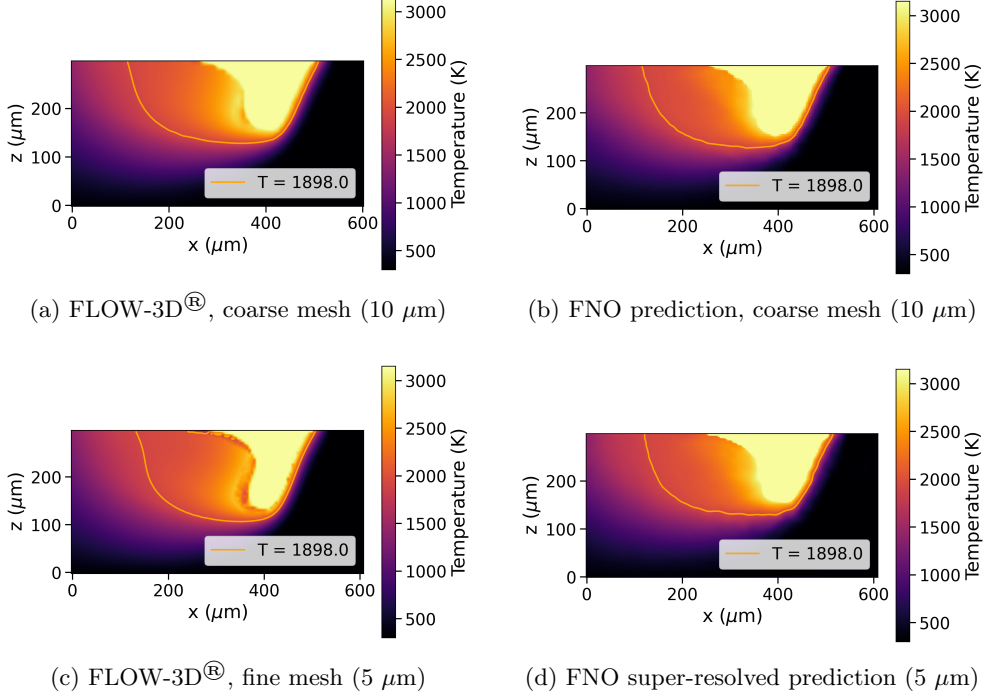


Fig. 9 Keyhole-regime melt-pool mid-point cross-section comparison for a test case with $P = 150.0$ and $V_{\text{scan}} = 0.54 \text{ m s}^{-1}$. The fine-resolution FNO result is obtained by super-resolving a model trained exclusively on coarse ($10 \mu\text{m}$) data. The visible discrepancy between coarse and fine FLOW-3D solutions indicates that mesh convergence has not yet been achieved at $10 \mu\text{m}$ resolution in the keyhole regime. This shows that while useful, FNO super-resolution can only be as good as its training data fidelity

set in [Figure 9](#). In both cases we see that the super-resolved FNO inference is essentially a finer representation of the coarse inference result. This is expected, and as such, the result is as accurate as the training set was accurate. Hence we have good agreement in the conduction mode simulation, since the corresponding coarse and fine Flow-3D simulations are close to each other. However, for the keyhole mode, we see the fine Flow-3D simulation is slightly more complex than the coarse counterpart, and hence, the super-resolved FNO inference result cannot fully capture the complexity of the fine Flow-3D reference simulation. While the FNO enables numerical super-resolution, it cannot recover physical features absent from the coarse-mesh training data.

Looking at the super-resolution metrics in [Table 5](#), we see that the errors are roughly double that of the non-super-resolved case in [Table 4](#), as discussed the discrepancy primarily comes from the lack of mesh convergence for $10 \mu\text{m}$ mesh size training data in the keyhole regime. One training method to ensure true physical fidelity in all regimes, while keeping computational training cost reasonable would be to employ

a coarse-to-fine training strategy, where FNO is first trained on a lot of coarse data, then progressively fine tuned on finer meshed data for regimes where training data has not yet reached mesh convergence.

Table 5 FNO error metrics on the super-resolved test (see Figure 1 for split) data ($5\ \mu\text{m}$ mesh). Absolute temperature errors are reported in kelvin; relative errors are in percent. Relative metrics are not reported for α and f_l as they are dimensionless

| Metric | T (K) | Metal–Gas interface (α) | Melt-pool (f_l) |
|---------------|---------|----------------------------------|---------------------|
| Abs. mean | 31.8 | 0.0040 | 0.0081 |
| RMSE | 68.0 | 0.036 | 0.080 |
| Rel. mean [%] | 5.3 | – | – |
| Rel. RMSE [%] | 11.3 | – | – |
| IoU mean | – | 0.998 | 0.741 |
| IoU std | – | 0.0014 | 0.066 |

4 Conclusion

In this work, we presented the LP-FNO, an FNO surrogate model for predicting quasi-steady melt-pool characteristics in laser processing across a wide range of regimes, from conduction to stable keyhole welding. High-fidelity thermo-fluid simulations generated with FLOW-3D WELD[®] were used as ground truth, incorporating free-surface dynamics, phase change, recoil pressure, and laser ray tracing. By transforming the data into the moving laser reference frame and applying temporal averaging, the inherently transient problem was recast into a quasi-steady formulation suitable for operator learning.

The trained LP-FNO accurately predicts three-dimensional temperature fields as well as metal–gas and melt-pool interfaces directly from process parameters, achieving low absolute and relative errors and near-perfect segmentation performance for the metal–gas interface in a fraction of a second. Importantly, the model generalizes across the full process window, including the challenging transition from conduction to keyhole regimes, without retraining for new parameter combinations.

A key strength of the approach is its resolution-invariant formulation. We demonstrated that an FNO trained exclusively on coarse $10\ \mu\text{m}$ simulation data can be evaluated on a finer $5\ \mu\text{m}$ mesh, effectively performing super-resolution. In the conduction regime, where the underlying FLOW-3D simulations are already mesh-converged at coarse resolution, the super-resolved predictions remain highly accurate. In contrast, in the keyhole regime, discrepancies between coarse and fine reference simulations limit the achievable accuracy of super-resolved inference, highlighting that neural operator fidelity is fundamentally bounded by the quality and convergence of the training data.

These results indicate that LP-FNO provides a powerful, fast, and efficient surrogate modeling framework for laser welding, capable of delivering near-instantaneous

predictions of full three-dimensional fields over broad parameter ranges. Such models are well suited for applications including rapid process optimization, uncertainty quantification, and real-time digital twins.

Looking ahead, an important limitation of high-resolution 3D FNO surrogates is that their dominant trainable component, the dense spectral channel-mixing weights, can become a parameter and memory bottleneck as the number of retained modes and latent channels increases, especially when extending to richer physics or higher-fidelity meshes. A natural future direction is therefore to explore parameter-efficient spectral mixing, including hybrid quantum-classical variants where a configurable subset of Fourier-layer channel mixing is produced by a small, mode-shared parametrized quantum circuit rather than many independent dense matrices. The motivation for quantum circuits here is not near-term runtime acceleration, but representational efficiency [38]: parametrized quantum circuits can serve as compact nonlinear mixers with global interactions induced by entanglement and a trainable parameter count that can be largely decoupled from the number of Fourier modes, potentially improving the accuracy – parameter and generalization trade-offs under limited data. Early results in quantum Fourier neural operators and related hybrid operator learning designs suggest this is a feasible research direction [39, 40].

Statements and Declarations

The authors declare that they have no competing interests. We would like to thank EMPA and Terra Quantum AG for supporting this work.

References

- [1] Michaleris, P.: Modeling metal deposition in heat transfer analyses of additive manufacturing processes. *Finite Elements in Analysis and Design* **86**, 51–60 (2014) <https://doi.org/10.1016/j.finel.2014.04.003> . Accessed 2026-01-25
- [2] Mukherjee, T., Zhang, W., DebRoy, T.: An improved prediction of residual stresses and distortion in additive manufacturing. *Computational Materials Science* **126**, 360–372 (2017) <https://doi.org/10.1016/j.commatsci.2016.10.003> . Accessed 2026-01-25
- [3] Mukherjee, T., Wei, H.L., De, A., DebRoy, T.: Heat and fluid flow in additive manufacturing—Part I: Modeling of powder bed fusion. *Computational Materials Science* **150**, 304–313 (2018) <https://doi.org/10.1016/j.commatsci.2018.04.022> . Accessed 2026-01-25
- [4] Moreira, C.A., Chiumenti, M., Caicedo, M.A., Baiges, J., Cervera, M.: High-fidelity part-scale simulations in metal additive manufacturing using a computationally efficient and accurate approach. *Additive Manufacturing* **104**, 104748 (2025) <https://doi.org/10.1016/j.addma.2025.104748> . Accessed 2026-01-25

- [5] De, A., DebRoy, T.: A smart model to estimate effective thermal conductivity and viscosity in the weld pool. *Journal of Applied Physics* **95**(9), 5230–5240 (2004) <https://doi.org/10.1063/1.1695593> . Accessed 2026-01-26
- [6] Saldi, Z.S., Kidess, A., Kenjereš, S., Zhao, C., Richardson, I.M., Kleijn, C.R.: Effect of enhanced heat and mass transport and flow reversal during cool down on weld pool shapes in laser spot welding of steel. *International Journal of Heat and Mass Transfer* **66**, 879–888 (2013) <https://doi.org/10.1016/j.ijheatmasstransfer.2013.07.085> . Accessed 2026-01-26
- [7] Kamara, A.M., Wang, W., Marimuthu, S., Li, L.: Modelling of the Melt Pool Geometry in the Laser Deposition of Nickel Alloys Using the Anisotropic Enhanced Thermal Conductivity Approach. *Proceedings of the Institution of Mechanical Engineers, Part B: Journal of Engineering Manufacture* **225**(1), 87–99 (2011) <https://doi.org/10.1177/09544054JEM2129> . Accessed 2026-01-26
- [8] Li, Z., Kovachki, N., Azizzadenesheli, K., Liu, B., Bhattacharya, K., Stuart, A., Anandkumar, A.: Fourier Neural Operator for Parametric Partial Differential Equations. *arXiv. arXiv:2010.08895 [cs]* (2021). <https://doi.org/10.48550/arXiv.2010.08895> . <http://arxiv.org/abs/2010.08895> Accessed 2025-09-04
- [9] Raissi, M., Perdikaris, P., Karniadakis, G.E.: Physics-informed neural networks: A deep learning framework for solving forward and inverse problems involving nonlinear partial differential equations. *Journal of Computational Physics* **378**, 686–707 (2019) <https://doi.org/10.1016/j.jcp.2018.10.045> . Accessed 2025-09-04
- [10] Karniadakis, G.E., Kevrekidis, I.G., Lu, L., Perdikaris, P., Wang, S., Yang, L.: Physics-informed machine learning. *Nature Reviews Physics* **3**(6), 422–440 (2021) <https://doi.org/10.1038/s42254-021-00314-5> . Accessed 2026-01-25
- [11] Ko, T., Kim, H., Shin, Y., Kim, D., Lee, Y.H., Hong, J., Lee, S.H.: Review of Recent Additive Manufacturing and Welding Research with Application of Physics-Informed Neural Networks. *Journal of Welding and Joining* **42**(4), 357–365 (2024) <https://doi.org/10.5781/JWJ.2024.42.4.3> . Accessed 2025-10-22
- [12] Li, Z., Zheng, H., Kovachki, N., Jin, D., Chen, H., Liu, B., Azizzadenesheli, K., Anandkumar, A.: Physics-Informed Neural Operator for Learning Partial Differential Equations. *ACM / IMS Journal of Data Science* **1**(3), 1–27 (2024) <https://doi.org/10.1145/3648506> . Accessed 2025-09-04
- [13] Torres, E., Schiefer, J., Niepert, M.: Adaptive Physics-informed Neural Networks: A Survey. *arXiv. arXiv:2503.18181 [cs]* (2025). <https://doi.org/10.48550/arXiv.2503.18181> . <http://arxiv.org/abs/2503.18181> Accessed 2025-11-14
- [14] Lu, L., Jin, P., Karniadakis, G.E.: DeepONet: Learning nonlinear operators for identifying differential equations based on the universal approximation theorem of operators. *Nature Machine Intelligence* **3**(3), 218–229 (2021) <https://doi.org/>

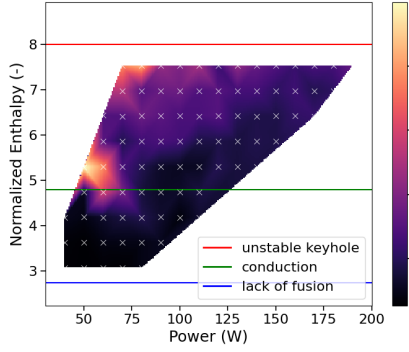
[10.1038/s42256-021-00302-5](https://doi.org/10.1038/s42256-021-00302-5) . arXiv:1910.03193 [cs]. Accessed 2025-09-04

- [15] Kovachki, N., Li, Z., Liu, B., Azizzadenesheli, K., Bhattacharya, K., Stuart, A., Anandkumar, A.: Neural Operator: Learning Maps Between Function Spaces With Applications to PDEs. *Journal of Machine Learning Research* **24**(89), 1–97 (2023)
- [16] Raonic, B., Molinaro, R., De Ryck, T., Rohner, T., Bartolucci, F., Alaifari, R., Mishra, S., Bezenac, E.: Convolutional Neural Operators for Robust and Accurate Learning of PDEs. In: *Advances in Neural Information Processing Systems (NeurIPS)* 36 (2023). <https://doi.org/10.48550/arXiv.2302.01178>
- [17] Manav, M., Perraudin, N., Lin, Y., Afrasiabi, M., Perez-Cruz, F., Bambach, M., De Lorenzis, L.: MeltpoolINR: predicting temperature field, melt pool geometry and their rate of change in laser powder bed fusion. *Journal of Intelligent Manufacturing* (2025) <https://doi.org/10.1007/s10845-025-02692-4> . Accessed 2026-01-08
- [18] Liu, N., Li, X., Rajanna, M.R., Reutzel, E.W., Sawyer, B., Rao, P., Lua, J., Phan, N., Yu, Y.: Deep neural operator enabled digital twin modeling for additive manufacturing. *Advances in Computational Science and Engineering* **2**(3), 174–201 (2024) <https://doi.org/10.3934/acse.2024010> . Accessed 2025-11-18
- [19] Safari, H., Wessels, H.: Physics-Informed Surrogates for Temperature Prediction of Multi-Tracks in Laser Powder Bed Fusion. arXiv. arXiv:2502.01820 [cs] (2025). <https://doi.org/10.48550/arXiv.2502.01820> . <http://arxiv.org/abs/2502.01820> Accessed 2025-11-18
- [20] Yaseen, M., Yushu, D., German, P., Wu, X.: Fast and accurate reduced-order modeling of a MOOSE-based additive manufacturing model with operator learning. *The International Journal of Advanced Manufacturing Technology* **129**(7-8), 3123–3139 (2023) <https://doi.org/10.1007/s00170-023-12471-1> . Accessed 2026-01-05
- [21] Hann, D.B., Iammi, J., Folkes, J.: A simple methodology for predicting laser-weld properties from material and laser parameters. *Journal of Physics D: Applied Physics* **44**(44), 445401 (2011) <https://doi.org/10.1088/0022-3727/44/44/445401> . Accessed 2026-01-07
- [22] FLOW-3D WELD®. Flow Science, Inc., Santa Fe, NM, USA (2025). <https://flow3d.com>
- [23] Svenungsson, J., Choquet, I., Kaplan, A.F.: Laser welding process—a review of keyhole welding modelling. *Physics procedia* **78**, 182–191 (2015)
- [24] Aggarwal, A., Shin, Y.C., Kumar, A.: Unravelling keyhole instabilities and laser

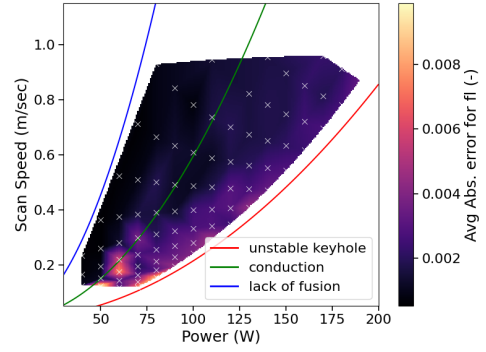
- absorption dynamics during laser irradiation of ti6al4v: A high-fidelity thermo-fluidic study. *International Journal of Heat and Mass Transfer* **219**, 124841 (2024)
- [25] Flint, T.F., Robson, J.D., Parivendhan, G., Cardiff, P.: laserbeamFoam: Laser ray-tracing and thermally induced state transition simulation toolkit. *SoftwareX* **21**, 101299 (2023) <https://doi.org/10.1016/j.softx.2022.101299> . Accessed 2025-09-16
- [26] Zenz, C., Buttazzoni, M., Florian, T., Armijos, K.E.C., Vázquez, R.G., Liedl, G., Otto, A.: A compressible multiphase mass-of-fluid model for the simulation of laser-based manufacturing processes. *Computers & Fluids* **268**, 106109 (2024)
- [27] Hemmasian, A., Ogoke, O.F., Akbari, P., Malen, J., Beuth, J., Barati Farimani, A.: Surrogate Modeling of Melt Pool Thermal Field Using Deep Learning. *Social Science Research Network, Rochester, NY* (2022). <https://doi.org/10.2139/ssrn.4190835> . <https://papers.ssrn.com/abstract=4190835> Accessed 2026-01-25
- [28] Ahn, S.-H., Song, I., Bae, J., Jeong, G.-H., Cho, D.-W., Park, Y.W.: A novel heat source model for welding and additive manufacturing: The traveling steady pool approach. *Journal of Manufacturing Processes* **153**, 471–486 (2025) <https://doi.org/10.1016/j.jmapro.2025.09.012>
- [29] Fulco, E., Coviello, D., Sargente, D.: Numerical analysis of the effect of stationary laser beam properties on Al-Si coating mixing in 22MnB5 steel. *International Journal of Heat and Mass Transfer* **255**(2), 127899 (2026) <https://doi.org/10.1016/j.ijheatmasstransfer.2025.127899>
- [30] Katinas, C., Shin, Y.C.: Prediction of initial transient behavior with stationary heating during laser powder bed fusion processes. *International Journal of Heat and Mass Transfer* **153**, 119663 (2020)
- [31] Li, Z., Huang, D.Z., Liu, B.: Fourier Neural Operator with Learned Deformations for PDEs on General Geometries. *Journal of Machine Learning Research* **24**(388), 1–26 (2023)
- [32] Hendrycks, D., Gimpel, K.: Gaussian Error Linear Units (GELUs). *arXiv. Version Number: 5* (2016). <https://doi.org/10.48550/ARXIV.1606.08415> . <https://arxiv.org/abs/1606.08415> Accessed 2026-01-25
- [33] Bischof, R., Kraus, M.A.: Multi-Objective Loss Balancing for Physics-Informed Deep Learning. *Computer Methods in Applied Mechanics and Engineering* **439**, 117914 (2025) <https://doi.org/10.1016/j.cma.2025.117914> . Accessed 2026-01-25
- [34] Kurz, W., Fisher, D.J., Rappaz, M.: *Fundamentals of Solidification 5th Fully Revised Edition*. *Foundations of Materials Science and Engineering*; 103, vol. 103. *Trans Tech Publications Ltd, ???* (2023). <https://doi.org/10.4028/b-v7b35q> . <https://infoscience.epfl.ch/handle/20.500.14299/245295>

- [35] Contributors, P.: NVIDIA PhysicsNeMo: An open-source framework for physics-based deep learning in science and engineering (2023). <https://github.com/NVIDIA/physicsnemo>
- [36] Chen, X., Liang, C., Huang, D., Real, E., Wang, K., Liu, Y., Pham, H., Dong, X., Luong, T., Hsieh, C.-J., Lu, Y., Le, Q.V.: Symbolic Discovery of Optimization Algorithms. arXiv. arXiv:2302.06675 [cs] (2023). <https://doi.org/10.48550/arXiv.2302.06675> . <http://arxiv.org/abs/2302.06675> Accessed 2026-01-27
- [37] Ahrens, J., Geveci, B., Law, C.: ParaView: An End-User Tool for Large-Data Visualization. Elsevier (2005). <https://doi.org/10.1016/B978-012387582-2/50038-1> . <https://linkinghub.elsevier.com/retrieve/pii/B9780123875822500381> Accessed 2026-01-27
- [38] Sedykh, A., Podapaka, M., Sagingalieva, A., Pinto, K., Pflictsch, M., Melnikov, A.: Hybrid quantum physics-informed neural networks for simulating computational fluid dynamics in complex shapes. Machine Learning: Science and Technology **5**(2), 025045 (2024) <https://doi.org/10.1088/2632-2153/ad43b2>
- [39] Jain, N., Landman, J., Mathur, N., Kerenidis, I.: Quantum Fourier Networks for Solving Parametric PDEs (2023). <https://arxiv.org/abs/2306.15415>
- [40] Marcandelli, P., He, Y., Mariani, S., Siena, M., Markidis, S.: Partitioned Hybrid Quantum Fourier Neural Operators for Scientific Quantum Machine Learning. In: 2025 International Conference on Quantum Computing and Engineering (2025). <https://doi.org/10.1109/QCE65121.2025.00185>

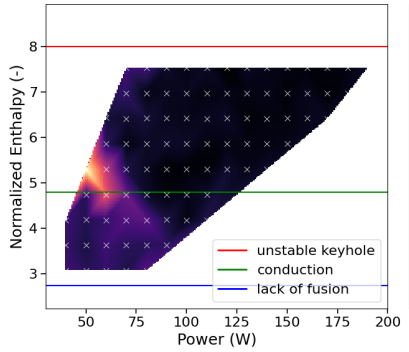
Appendix A Extra figures on LP-FNO Convergence and Hyperparameters



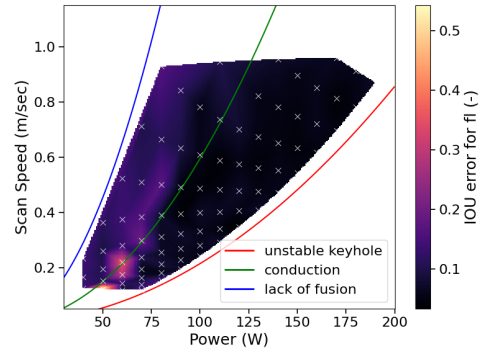
(a) Avg. absolute error for f_l ($P-H$)



(b) Avg. absolute error for f_l ($P-V_{scan}$)

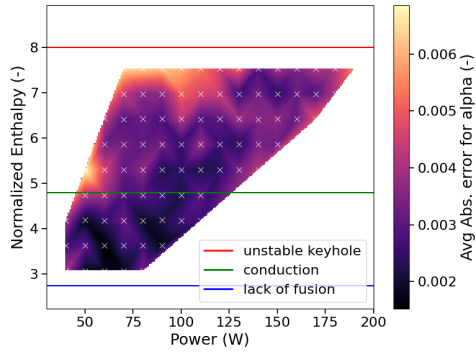


(c) IoU error ($1-IoU$) for f_l ($P-H$)

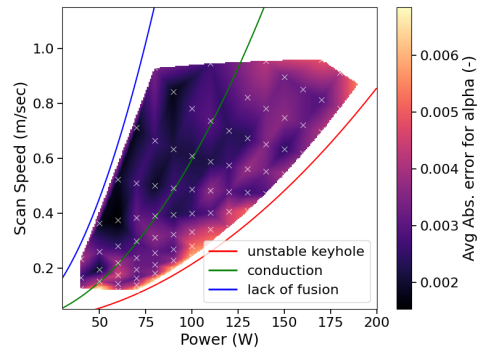


(d) IoU error ($1-IoU$) for f_l ($P-V_{scan}$)

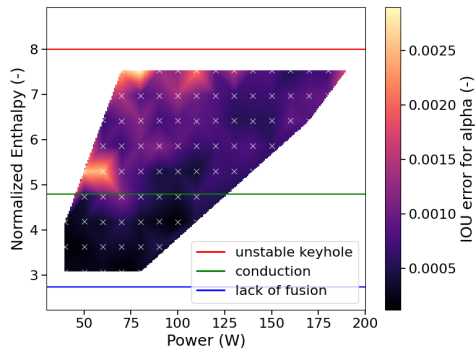
Fig. 10 Melt-pool (liquid fraction f_l) segmentation performance across the process window. Top row: average absolute error. Bottom row: IoU error ($1-IoU$) computed after thresholding at $f_l \geq 0.5$. Results are shown in two parameterizations: (P, V_{scan}) and (P, H). Good segmentation overall, except for one outlier at $P = 50$ W, $V_{scan} = 0.122$ m/s, which lies at edge of data in start of conduction-keyhole transition



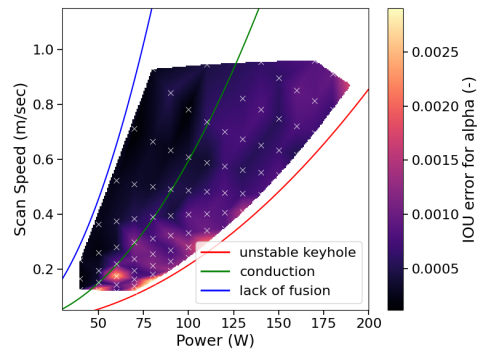
(a) Avg. absolute error for α ($P-H$)



(b) Avg. absolute error for α ($P-V_{scan}$)

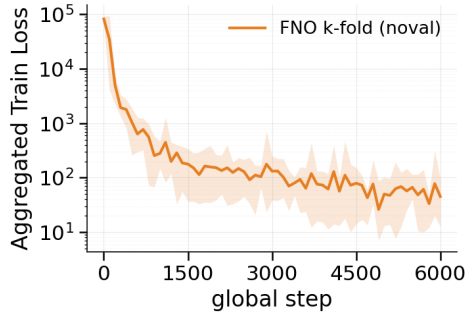


(c) IoU for α ($P-H$)

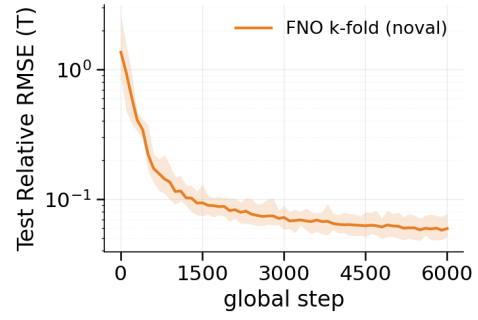


(d) IoU for α ($P-V_{scan}$)

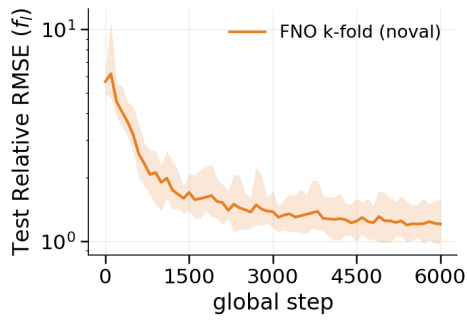
Fig. 11 Metal–gas interface (α) segmentation performance across the process window. Top row: average absolute error. Bottom row: IoU computed after thresholding at $\alpha \geq 0.5$. Results are shown in two parameterizations: (P, H) (left) and (P, V_{scan}) (right)



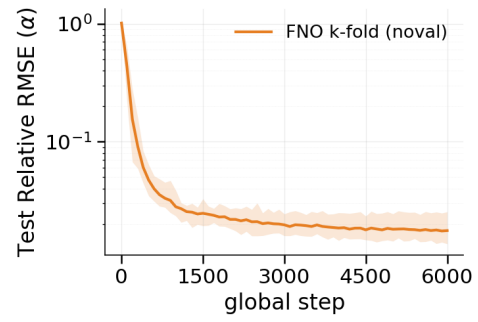
(a) Aggregated training loss



(b) Temperature Rel. RMSE



(c) Liquid fraction (f_l) Rel. RMSE



(d) Solid Fraction (α) Rel. RMSE

Fig. 12 LP-FNO training k-fold convergence metrics for dataset omitting validation set simulations. Across all outputs, consistent convergence is observed during training

Table 6 FNO architecture and training hyperparameters

| Category | Parameter | Value |
|------------------------------------|------------------------------------|-------------------------------|
| <i>FNO encoder</i> | | |
| | Spatial dimension | 3 |
| | Number of FNO layers | 3 |
| | Fourier modes per dimension | [25, 20, 15] |
| | Padding | 9 (constant) |
| | Activation function | GELU |
| | Coordinate features | enabled |
| | Input variables | $x, y, z, V_{\text{scan}}, P$ |
| <i>Decoder (pointwise network)</i> | | |
| | Architecture | convolutional fully connected |
| | Number of layers | 3 |
| | Hidden layer width | 32 |
| | Activation function | SiLU |
| | Weight normalization | enabled |
| | Skip connections | disabled |
| | Output variable | T |
| <i>Loss aggregator (ReLoBRaLo)</i> | | |
| | α | 0.95 |
| | β | 0.99 |
| | τ | 3.0 |
| | ε | 1×10^{-8} |
| <i>Optimization</i> | | |
| | Optimizer | Lion |
| | Learning rate | 6×10^{-5} |
| | β coefficients | (0.9, 0.99) |
| | Weight decay | 0 |
| <i>Learning-rate schedule</i> | | |
| | Scheduler | exponential decay |
| | Decay rate | 0.98 |
| | Decay steps | 100 |
| <i>Training setup</i> | | |
| | Maximum training steps | 6000 |
| | Gradient clipping norm | 0.5 |
| | Batch size (training / validation) | 1 / 5 |